Effects of phase synchronization on the tonal sound directivity of distributed propellers

Original
Effects of phase synchronization on the tonal sound directivity of distributed propellers / Zarri, A.; De Prenter, F.; Avallone, F.; Ragni, D.; Casalino, D.. - In: THE JOURNAL OF THE ACOUSTICAL SOCIETY OF AMERICA. - ISSN 1520-8524. - 157:5(2025), pp. 3267-3281. [10.1121/10.0036557]

Publisher:
American Institute of Physics

Published
DOI:10.1121/10.0036557

JASA ARTICLE

Effects of phase synchronization on the tonal sound directivity of distributed propellers[a]

A. Zarri,[1,2,b] F. de Prenter,[1] F. Avallone,[3] D. Ragni,[1] and D. Casalino[1]

[1]*Department of Flow Physics and Technology, Delft University of Technology, Kluyverweg 1, 2629 HS Delft, The Netherlands*

[2]*Aeronautics and Aerospace Department, von Karman Institute for Fluid Dynamics, Waterloosesteenweg 72, B-1640 Sint-Genesius-Rode, Belgium*

[3]*Department of Mechanical and Aerospace Engineering, Politecnico di Torino, 10129 Torino, Italy*

ABSTRACT:

Recent studies on distributed electric propulsion systems suggest phase synchronization between rotors as a noise reduction strategy. However, the aerodynamic interactions between propellers' near fields and their influence on far-field tonal noise remain poorly understood, partly due to experimental limitations in microphone placement. This paper addresses this gap through lattice Boltzmann very large eddy simulations of three adjacent, co-rotating rotors, spaced radially at 2% of their diameter, to investigate how relative phase angle affects tonal noise directivity. Results reveal that proximity-induced aerodynamic interactions generate dominant tonal noise in most spatial directions, driven by two mechanisms: time-averaged inflow distortion from nearby propellers and impulsive local effects at blade tips, with the latter influenced by phase angle. While the directivity pattern of the blade-passing frequency harmonic tone remains consistent across phase angles, comparing cases with zero relative phase (blades aligned) and opposite-phase conditions shows sound pressure level shifts of up to 4.5 dB along the primary noise axis, namely, along the inflow direction. Conversely, acoustic interference significantly alters noise directivity, especially in opposite-phase conditions where sound is nearly canceled in specific directions. These findings highlight rotor synchronization as a promising strategy for reducing noise emissions toward sensitive areas.

https://doi.org/10.1121/10.0036557

(Received 5 December 2024; revised 11 April 2025; accepted 12 April 2025; published online 1 May 2025)

[Editor: James F. Lynch] Pages: 3267–3281

I. INTRODUCTION

The emergence of urban air mobility (UAM) and the proliferation of small-scale unmanned aerial vehicles have driven research focused on novel propulsion systems that need to minimize environmental impact while enhancing operational efficiency. Distributed electric propulsion (DEP) systems, which consist of arrays of electrically driven propellers, have emerged as a promising solution to offer potential improvements in aerodynamic efficiency and reductions in pollutant emissions (NASA, 2017; Teets *et al.*, 2002). DEP configurations facilitate advanced aircraft designs by distributing thrust generation across multiple propellers along the wingspan, thus providing benefits such as spanwise lift augmentation and enhanced low-speed performance (Kim *et al.*, 2018; Kummer and Dang, 2006).

However, when propellers are positioned nearby, as often for DEP systems, the interactions between these propellers can give rise to complex aerodynamic and acoustic phenomena (Zarri *et al.*, 2022b). These interactions exacerbate noise levels and pose significant challenges to both human comfort and regulatory compliance. The close spacing between propellers leads to aerodynamic blade load oscillations (which are enhanced when the propellers get closer) and an increase in both tonal and broadband noise components (Lee and Lee, 2020; Zhou *et al.*, 2017). Such noise emissions, if not adequately controlled, could hinder the integration of UAM and DEP technologies into urban environments or reduce the benefits obtained with other noise reduction technologies. Consequently, understanding and mitigating noise generated by DEP systems is critical for their future adoption and ensuring sustainable urban air transportation (Patterson *et al.*, 2020).

Whether in an isolated propeller (IP) or distributed configuration (DP), the tonal noise emissions produced at the blade passing frequency (BPF) of the propeller and its higher harmonics are the primary contributors to noise discomfort and annoyance (Zang *et al.*, 2024; Torija *et al.*, 2021). These acoustic emissions are driven by sound generation mechanisms that stem from either intrinsic properties related to the propeller's geometry and kinematics or from interactions between propeller and adjacent components (Roger and Moreau, 2020; Barker *et al.*, 2023), inflow vortical disturbances (Casalino *et al.*, 2019b; Casalino *et al.*, 2023), and inflow distortion (Romani *et al.*, 2022b). In the

---

[a]This paper is part of a special issue on Advanced Air Mobility Noise: Predictions, Measurements, and Perception.

[b]Email: a.zarri@tudelft.nl

first scenario, two main types of noise are identified: thickness noise and steady loading noise. The former arises from the displacement of air by the rotating blades, which is essentially a result of the physical presence and movement of the blades through the air. Steady loading noise, on the other hand, is generated by the steady aerodynamic forces moving in space due to the propeller rotation. Both types of noise occur even when the propeller operates in isolated conditions with a uniform inflow.

Differently, aerodynamic installation effects occur when the propeller is subjected to unsteady loads due to interactions with other propellers, the airframe, or non-uniform inflow conditions. The latter case can also interest an IP, for instance, in the presence of a non-zero angle between the rotor disk and the inflow velocity. At low Mach numbers, these effects can easily dominate tonal noise emissions (Glegg and Devenport, 2017), particularly for the tonal content present at the BPF harmonics. While these aerodynamic interactions generally have a minimal effect on the overall aerodynamic performance of propellers in forward flight (de Vries *et al.*, 2021), Bernardini *et al.* (2020) demonstrated that, in DEP systems, unsteady loading noise becomes dominant when adjacent propellers are spaced closer than 2.5% of their diameter. Similarly, the interaction among near propellers was proven to have a significant impact on noise emission and was thoroughly studied, especially in hover conditions, in recent years (Lee and Lee, 2020; Zarri *et al.*, 2022a; Intaratep *et al.*, 2016; Pascioni and Rizzi, 2018).

One way to mitigate noise emissions is by synchronizing the rotation of the rotors to maintain a constant relative phase angle.

Several studies have investigated the effects of propeller phase synchronization on noise reduction in hover conditions. Pascioni *et al.* (2019) examined a three-bladed propeller operating at 5100 rpm with a 16-in. diameter, employing both numerical and experimental methods, resulting in a noise reduction of 6 dB at the BPF harmonic. Shao *et al.* (2022) experimentally examined a two-bladed propeller with a 12-in. diameter and at 4000 rpm, with noise reductions reported between 1 and 11 dB. Guan *et al.* (2021) used numerical methods to study a two-bladed propeller at 6000 rpm with a 12.5-in. diameter, considering hovering and low-speed flight conditions (advance ratio between 0 and 0.1), and reported noise reductions with single-probe measurement ranging from 11 to 30 dB. Notably, these studies have furthermore shown that blade clocking has a negligible impact on the rotors' thrust production capabilities. Recently, experimental work was conducted for forward-flight conditions too: Turhan *et al.* (2024) investigated a two-bladed propeller and, with a relative phase angle of 90°, observed noise reductions of about 24 dB at the first BPF harmonic. De Paola *et al.* (2024) with four-bladed propellers experimentally achieved a reduction of about 5 dB at the first BPF harmonic. Some of the previous studies pointed to acoustic interference effects, also known as acoustic installation effects, as a primary mechanism for this noise reduction in DEP. These effects arise from the interaction between the acoustic fields of adjacent noise sources. When sound waves from these sources overlap, they can either constructively interfere, amplifying noise, or destructively interfere, reducing the perceived noise levels (Zarri *et al.*, 2022a). Unlike aerodynamic installation effects, which depend on airflow dynamics, acoustic interference effects are determined by the phase relationships and spatial alignment of the sound waves as they propagate and reach the listener in the far field (Roger *et al.*, 2022).

The reported noise reductions for both hovering and forward-flight cases span a remarkably wide range, sometimes up to 30 dB, even within similar experimental setups. This scattering can be partly explained by the challenges inherent in experimental measurements. In many cases, only a few microphones are deployed at discrete locations to capture the propellers' sound pressure level (SPL). Since phase synchronization has a profound effect on the noise directivity of tonal components, a measurement taken at one specific location might indicate a dramatic reduction due to destructive interference, while another might not capture the same effect. Ideally, a spherical array of microphones should always be used to measure the complete spatial distribution of the SPL, thus providing an unambiguous reflection of the overall noise reduction by computing the sound power level (SWL). However, this approach is challenging to implement in experimental settings. The present study circumvents these limitations by employing numerical simulations, which facilitate the estimation of the total SWL without the spatial constraints associated with physical microphone placement.

The aim of this study, which focuses on adjacent co-rotating and phase-synchronized propellers, is to determine whether the reduced sound levels observed in the literature are primarily due to aerodynamic installation effects, acoustic interference, or a combination of both. This understanding will offer deeper insights into the mechanisms behind noise generation and explore whether phase synchronization can be effectively leveraged as a noise mitigation technique. High-fidelity simulations will be employed, as they allow isolating aerodynamic installation effects from acoustic interference effects, unlike experimental techniques. The approach of this analysis is similar to the work done in Zarri *et al.* (2022a) on a hovering drone.

A parametric study based on the relative phase angle will help identify which configurations exhibit lower emissions and clarify the underlying physics of this interaction, which remain not fully understood. This analysis will also enable the characterization of the directivity of acoustic emissions from DEP systems, determining whether there are specific spatial directions in which steady loading noise remains significant compared to unsteady loading noise. Understanding the relative dominance of sound mechanisms in terms of spatial directivity is crucial for reducing noise levels in specific regions, such as mitigating sound impact in the direction of the ground, where listeners are typically located.

The structure of this document is as follows. Section II provides an overview of the numerical methods used for flow-field and far-field noise calculations and a detailed description of the computational configuration involving three adjacent propellers. In Sec. III, the aerodynamic simulations are validated through comparison with experimental data. Section IV examines the flow characteristics for both isolated and distributed propulsion systems. Section V covers the acoustic results while Sec. VI provides a summary of the results and suggests directions for future research.

II. MATERIAL AND METHODS

A. Computational methodology

The flow around the propellers and the sound radiations are simulated using the commercial computational fluid dynamics (CFD) and computational aeroacoustics software SIMULIA PowerFLOW®, version 6-2021-R2. This software employs the lattice Boltzmann (LB) method to solve the discrete LB equation for the particle distribution function, denoted as $f(\boldsymbol{x}, \boldsymbol{v}, t)$. This function describes the probability density of particles with velocity $\boldsymbol{v}$ at a given location $\boldsymbol{x}$ and time t. The simulation is performed using a D3Q19 stencil, which incorporates 19 discrete velocity directions in three spatial dimensions, coupled with a regularized collision operator derived from the Bhatnagar–Gross–Krook (BGK) model (Bhatnagar *et al.*, 1954). The discrete distribution function is integrated to compute flow parameters like density and velocity (Shan and Chen, 2006). For cases involving high-subsonic Mach numbers, where the local Mach number exceeds or is close to 0.5, such as in this study, the LB solver is coupled with an energy conservation equation. This equation is solved using a Lax–Wendroff finite difference method on the Cartesian LB grid (Nie *et al.*, 2009).

The LB equations are solved on a Cartesian grid comprising cubic volumetric elements (voxels), while surfaces of solid objects are discretized using planar surface elements (surfels) within each voxel that intersects the geometry. The no-slip and slip wall boundary conditions are implemented via a boundary mechanism based on a particle bounce-back process and a specular reflection process, respectively (Chen *et al.*, 1998).

The solver applies a very large eddy simulation (VLES) approach to account for unresolved turbulent scales. This involves a two-equation turbulence model based on the k-ϵ renormalization group theory (Yakhot and Orszag, 1986), which determines the turbulent relaxation time corresponding to the resolved flow field's shear time scales (Romani and Casalino, 2019). In turbulent flows, this relaxation time is a key factor in the collision process of the kinetic model, which aligns with the local levels of turbulent kinetic energy at equilibrium. As discussed by Casalino *et al.* (2022), combining a kinematic gas model with a turbulence transport model affects both the collision process and the equilibrium distribution function of a so-called "gas of eddies." Moreover, the dynamic adjustment of inherent shear-flow time scales is a key element in the simulation of transitional flows.

To reduce the computational cost associated with solid-wall mesh refinement, a pressure-gradient extended wall model is employed to approximate the no-slip boundary condition on solid walls (Avallone *et al.*, 2018a). This model extends the generalized law of the wall to incorporate pressure gradient effects.

Far-field noise predictions are computed using an impermeable Ffowcs Williams–Hawkings (FW–H) formulation, specifically Farassat's Formulation 1A (F1A) (Farassat, 2007), which is solved forward in time (Casalino, 2003) and implemented in the post-processing software SIMULIA PowerACOUSTICS® and SIMULIA OptydB®, the latter providing additional capabilities in terms of noise source identification. This approach involves the calculation of surface integrals over solid surfaces to compute acoustic monopoles and dipoles, which correspond to thickness and loading noise, respectively. The quadrupole terms, representing non-linear effects such as turbulence mixing, shock waves, and non-linear propagation, are omitted since they are insignificant for propellers operating at low blade-tip Mach numbers (Goldstein, 1976; Glegg and Devenport, 2017).

B. Setup of the simulations

The computational setup is based on experiments conducted in de Vries *et al.* (2021), which involve a configuration with three adjacent propellers, referred to as TUD-XPROP-S propellers, each having six blades and a diameter of $D = 0.2032\,\mathrm{m}$. The geometry for these propellers was provided by the Delft University of Technology. The propellers have a pitch angle of 30° at 70% of the radius R with a root chord length of $c_r = 16.287\,\mathrm{mm}$. Additional details on the pitch angle and chord length distribution along the blade span are available in de Vries *et al.* (2021).

The propeller and spinner geometries are accurately replicated from the experiments; however, the wind tunnel test section is excluded from the computational domain. Similarly, the supports used to hold the nacelles during the measurements are not included. The nacelles themselves are designed with a length of $3.7R$ and are tapered at their ends to minimize any disturbance to the flow field around the rotors.

The propellers are arranged along the Y axis as shown in Fig. 3(a), with a tip clearance of $\delta = 0.02D = 4.064\,\mathrm{mm}$. The global reference system (GRS) (X, Y, Z) is also depicted in this figure. The propellers rotate in the same direction (anticlockwise) with a relative phase angle of $\Delta\phi = 0^\circ$. To examine the impact of the relative phase angle on aerodynamic and acoustic performance, other configurations are simulated with $\Delta\phi = 10^\circ, 20^\circ, 30^\circ, 40^\circ, 50^\circ$. All of these simulations have been performed on the Dutch National Supercomputer Snellius.

They are conducted with a free-stream velocity of $V_\infty = 30\ \mathrm{m\ s^{-1}}$ along the X axis, corresponding to an advance ratio of $J = V_\infty/(ND) = 0.8$, where N is the number of rotations per second. The Mach number at the blade tip is 0.357, and the Reynolds number is 5.66×10^4, considering a tip chord length of 6.8 mm. The free-stream conditions are a static pressure of $p_\infty = 101\,330$ Pa and a temperature of $T_\infty = 288.15$ K, with inlet turbulence intensity set to 0.04%, similar to the experimental conditions. The rotation period is $T_{rot} = 5.42 \times 10^{-3}$ s, corresponding to the angular velocity $\Omega = 11\,073$ rpm.

Differently from the experiments, zig-zag tripping devices are located on the suction side of the blades to force a turbulent boundary-layer transition, prompting the VLES method to switch from modeled- to resolved-scale modality. This approach, validated in previous studies (Avallone *et al.*, 2018b; Casalino *et al.*, 2019a), constitutes a low computational cost alternative to a wall-mesh refinement below a y^+ value of about 15, as required to resolve a transitional boundary layer flows (Casalino *et al.*, 2022) accurately. As shown by Goyal *et al.* (2024), for y^+ larger than 15, the adoption of a wall model in the lattice Boltzmann method-very large eddy simulation (LBM-VLES) for transitional flow can cause errors in the estimation of both thrust and torque that can be avoided by using the zig-zag trip and considering the flow fully turbulent.

The zig-zag trip is constructed using the OptydB® toolkit within the PowerFLOW rotor noise workflow (Casalino *et al.*, 2021), featuring a chordwise amplitude of $0.05c_r$, a spanwise distance between subsequent peaks of $0.1c_r$ and a height of about $3.3 \times 10^{-3}c_r$.

The computational domain, illustrated in Fig. 1(a), is a cubic volume with each side located 64D away from the GRS origin. An acoustic sponge, or anechoic layer, is defined between two concentric spheres with radii $8D$ and $30D$, respectively, to prevent acoustic reflections at the boundaries (Avallone *et al.*, 2018a; Romani *et al.*, 2022a). In this region, viscosity is gradually increased until it reaches a constant value beyond $30D$. A total of 14 variable resolution (VR) regions are used, with a resolution change factor of 2 between adjacent regions. The initial eight VR regions are centered around the GRS origin, with increasing refinement levels as they approach the origin. In Fig. 1(b), the local reference frame of each propeller is defined by three volumes of revolution, which slide relative to the stationary outer grid. These are linked to cylindrical hollow regions at VR9 to discretize the regions around the slipstream helical paths accurately. The refinement around the blade and spinner surfaces, as well as ring regions that follow the blade tip motion, is set as VR10 [Fig. 1(b)], ensuring at least four voxels are used to discretize gaps between the rotating blade tips. Higher refinements, VR10 to VR12, are applied directly on the blade surfaces to model the boundary layer accurately (see Fig. 2), while VR9 envelopes the nacelles. The finest refinements, VR13 and VR14, cover the zig-zag trip device positioned at 10% from the blade leading edge [Fig. 3(b)], to discretize the trip thickness with about three voxels, in accordance with guidelines from Casalino *et al.* (2021). VR14 contains the smallest voxels with a size of 1.79445×10^{-5} m. The wall-resolved grid is designed to ensure that y^+ remained around 15 across most of the blade surface.

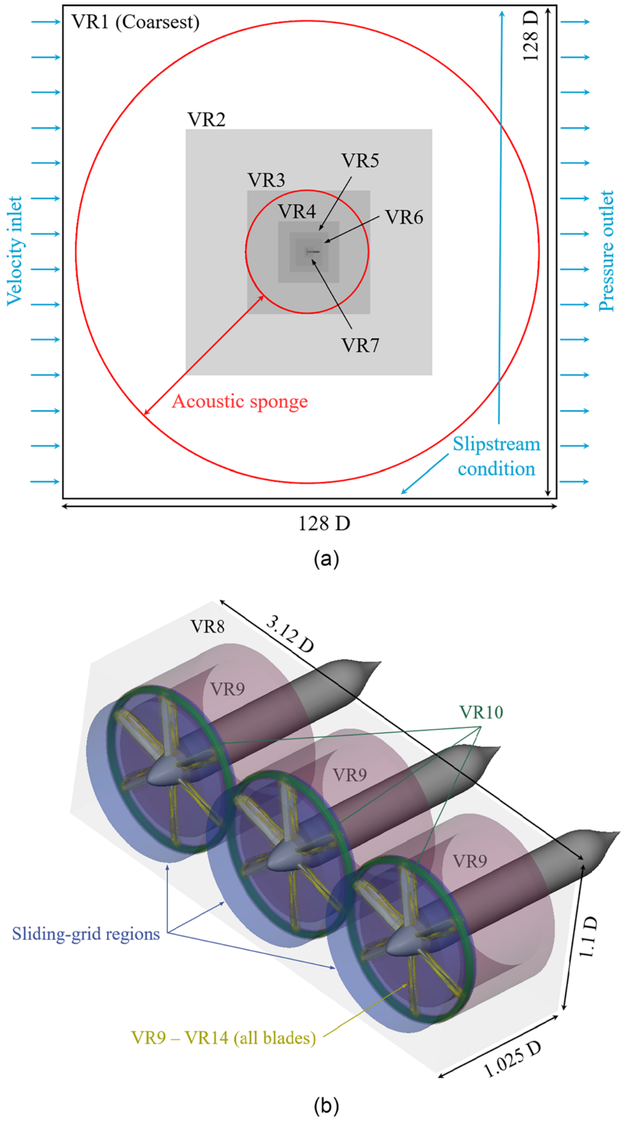

FIG. 1. (a) Side view of the computational domain with the VR grid regions and the boundary conditions. (b) Close-up view of the domain illustrating the distribution of VR regions near the propellers.

The finest grid setup uses approximately 225.5×10^6 voxels, with a VR14 resolution corresponding to 900 voxels per characteristic length (c_r). The IP case shares the same setup and characteristics but with roughly a third of the total voxel count. The CPU time needed for IP and DP simulations amounts to approximately 37 000 and 112 000 CPU hours, respectively.

Wall-pressure fluctuations on the propeller blades are sampled at 33.22 kHz and used as the solid FW–H integration surface. This sampling rate ensures sufficient time resolution up to the tenth harmonic of the BPF, with a Nyquist safety factor of 3 to prevent aliasing artifacts. The sampling time step corresponds exactly to 2° of blade rotation, ensuring that each blade passage is captured by an integer number of sampling points and that sampling moments remain synchronized across passes. As expected, the F1A far-field analysis results in a highly periodic signal dominated by tonal components. Therefore, spectral properties are derived by

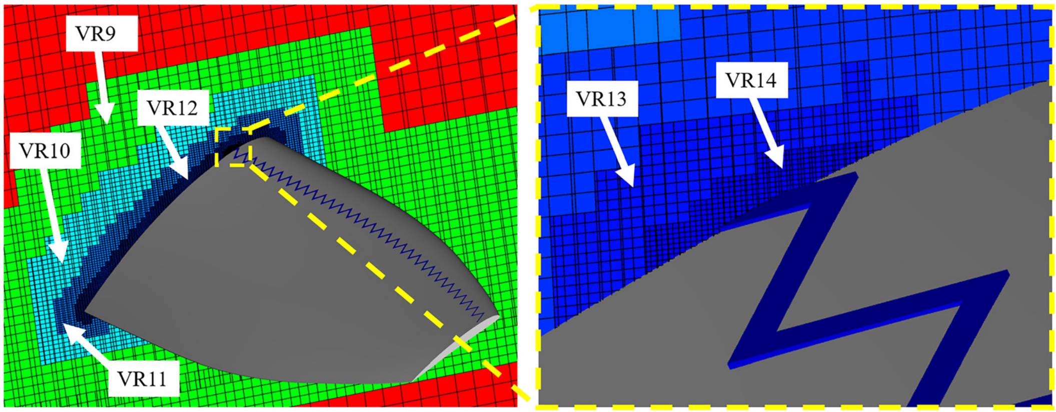

FIG. 2. On the left, a close view of VR9, 10, 11, and 12 is provided, together with their voxel size. To the right, a zoom on the zig-zag tripping device region is shown to highlight VR13 and 14.

applying a fast Fourier transform (FFT) directly to a time-domain signal that spans an integer number of rotations [see Fig. 5(b)]. Since the signal is perfectly periodic, a Hanning-type window is not required. Typically, a window is used to mitigate spectral leakage when a tone's energy spreads across adjacent FFT bins. However, because the tonal (BPF) frequencies align exactly with the FFT bins in this case, all of the energy is confined to single bins. This precise capture eliminates the need to integrate over a small bandwidth, and computing the FFT at the shaft/BPF harmonic frequencies produces the same result as performing phase-averaging on the time-domain signal. For the subsequent results, a moving dipole formulation is used to compute the pressure amplitudes of the tonal noise. The SPL of these tones is computed from the obtained amplitudes ($p_{\mathrm{BPF_n}}$) by

$$L_p(f) = 10\log_{10}\frac{0.5p^2_{\mathrm{BPF_n}}}{p^2_{ref}},$$

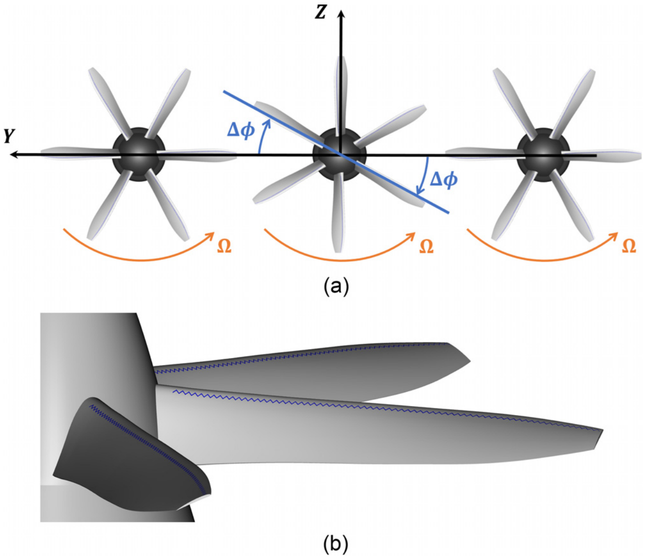

FIG. 3. (a) Front view of the array of propellers defining the global reference frame, angular velocity Ω, and relative phase angle $\Delta\phi$. (b) Close-up on the zig-zag tripping applied on the blades.

which yields the acoustic decibels output. $p_{ref} = 20\,\mu$Pa is the reference pressure. To compute the SWL, a spherical array of 2500 microphones is positioned around the propeller at a distance of 100D from the origin to accurately capture the sound field in all directions. It was verified that by increasing the number of microphones as well as the distance from the origin, the obtained SWL remained constant. The root mean square (RMS) pressure was calculated over all microphone positions. The RMS pressure squared p^2_{rms} is obtained as the mean square of the pressure levels at the chosen BPF harmonic across all microphone positions. The sound power emitted by the source is then computed: $\mathrm{W} = p^2_{\mathrm{rms}}A_m/\rho_\infty c_\infty$, where ρ_∞ is the air density, c_∞ is the speed of sound in air, and the area $A_m = 4\pi R^2_m$ corresponds to the surface area of the sphere formed by the microphone array, with R_m being the distance from the source to each microphone. Finally, SWL is calculated as

$$\mathrm{SWL} = 10\log_{10}\left(\frac{\mathrm{W}}{\mathrm{W_{ref}}}\right),$$

where $\mathrm{W_{ref}} = 1\times10^{-12}$W is the reference sound power. This expression provides the SWL in decibels, representing the total acoustic power radiated by the source in all directions.

C. Rotating-dipole formulation

To accelerate the computation of tonal noise harmonics for the spherically distributed 2500 microphones (see Sec. V), the solid FW–H integral is replaced by a chordwise compact dipole formulation. This approach is valid since the wavelengths of the considered tones are much larger than the chords of the blades. Hereby, the loading of each blade is replaced by 50-point forces (i.e., dipoles) evenly distributed along the span, corresponding to the integrated forces over span-wise blade segments. These forces are obtained from the blade-loading harmonics (BLHs), described in Sec. II D. The frequency-domain formulation of the far-field noise in this manner was initially introduced by Hanson (1976), and the exact formulation was taken from

Schram (2011) and enhanced with radial forces. The formulation is written as

$$\begin{aligned}\hat{P}(mB\Omega) &= \frac{-\mathrm{i}B^2\Omega e^{-\mathrm{i}mB\Omega R_{\mathrm{mic}}/c_\infty}}{4\pi R_{\mathrm{mic}}c_\infty}e^{-\mathrm{i}mB\phi}\\ &\quad\times\sum_{n=-\infty}^{n=\infty}e^{-\mathrm{i}(mB-n)(\zeta-\pi/2)}(J_{mB-n}(mBM\sin(\theta))\\ &\quad\times\left(m\cos(\theta)\hat{F}_t(n\Omega)-\frac{mB-n}{BM}\hat{F}_d(n\Omega)\right)\\ &\quad-J'_{mB-n}(mBM\sin(\theta))\mathrm{i}m\sin(\theta)\hat{F}_r(n\Omega)),\end{aligned}\tag{1}$$

with the Fourier transforms of the acoustic pressure at the microphone position, the axial force, the tangential force, and the radial force of a dipole denoted by $\hat{P}(\cdot)$, $\hat{F}_t(\cdot)$, $\hat{F}_d(\cdot)$, and $\hat{F}_r(\cdot)$. The BPF harmonic of the observed noise is denoted by m; n is the shaft frequency harmonic of the loading (with numerically $-45 \leq n \leq 45$). $B = 6$ gives the number of blades, the microphone distance is R_{mic}, the Mach number of the segment/dipole is indicated by M, and $J_i(\cdot)$ indicates the ith Bessel function of the first kind. Figure 4(b) defines the angles ζ and θ, which indicate the direction of the microphone, while ϕ is the initial angle of the propeller as in Fig. 3(a). The model does not include thickness noise, which is negligible (Roger and Moreau, 2020), as confirmed in Sec. III B.

D. Computation of BLHs

Blade loading data are post-processed from the surface forces resulting from the LBM-VLES simulations. These surface forces are averaged over four timesteps (i.e., 1.1×10^{-7} s) and are saved for each surface element (surfel) for every 2° of rotation, resulting in 1800 frames for ten rotations. The measurements start after an initialization period of ten rotations on a coarse grid followed by two rotations on the fine grid. Blade loading data are extracted from the surface forces and converted to axial, tangential, and radial components in 70 radial segments spanning 1.2 mm for each blade and each frame. Next, a phase-locked average is computed for each angle and segment over all the blades and rotations. The discrete loading data for each radial segment and 2° azimuthal angle are then projected (in L^2) on a basis with ten uniform quadratic B-splines in the radial direction and 45 harmonics in the azimuthal direction, yielding a total of 910 degrees of freedom for each loading component, which is represented as

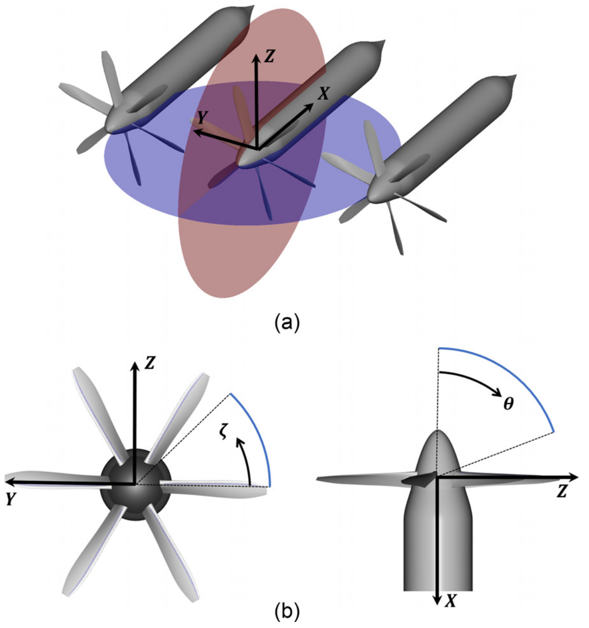

FIG. 4. (a) Definition of the microphone planes XY, XZ. (b) Definition of microphone angles θ and ζ.

$$f(r,\theta) = \sum_{1\leq k\leq 10}\sum_{0\leq n\leq 45}\alpha_{kn}S_k(r)\cos(n\theta+\gamma_{kn}),$$

with $f\,[\mathrm{N/m}]$ the loading component, $\alpha_k n \geq 0\,[\mathrm{N/m}]$ the magnitude of a loading contribution (460 degrees of freedom), and $0 \leq \gamma_{kn} < 2\pi$ the phase (450 degrees of freedom). Due to the orthogonality of harmonic modes, the projection on these is equivalent to a Fourier transform. The dipole to calculate the far-field noise is obtained by integrating the harmonic components over the radial segment corresponding to the respective rotating dipole

$$\hat{F}^{(s)}(n\Omega) = \sum_{1\leq k\leq 10}\alpha_{kn}e^{i\gamma_{kn}}\int_{r_s}S_k(r)\mathrm{d}r,$$

with $\hat{F}^{(s)}(n\Omega)[\mathrm{N}]$ the complex amplitude of the nth shaft harmonic of the dipole corresponding to the sth radial segment. r_s [m] denotes this segment in the integral.

III. VALIDATION

A. Simulated against experimental thrust

Figure 5(a) presents the results of the thrust coefficient evolution while progressively activating refined VRs for both the IP configuration (blue) and the DP configuration with a relative phase angle of $\Delta\phi = 0°$ (red). The thrust coefficient, defined as $T_c = T/(q_\infty \pi R^2)$, is used to quantify performance, where T represents thrust and q_∞ denotes the dynamic pressure in the undisturbed upstream flow.

All VRs higher than VR8 are deactivated for the coarser grid, while those above VR11 are turned off in the medium-resolution grid. The experimental results for both cases are depicted as dashed lines, with uncertainty ranges represented by shaded regions. The trend in the thrust coefficient becomes progressively closer to experimental measurements (de Vries *et al.*, 2021), achieving a final deviation of only 1.3% with the finest grid resolution for the IP. It must be specified that this technique does not represent a convergence study, as the grid density is not uniformly increased when finer VRs are activated. However, the evolution of the thrust value and the need for finer VRs up to VR14 are represented in order to approach the experimental value.

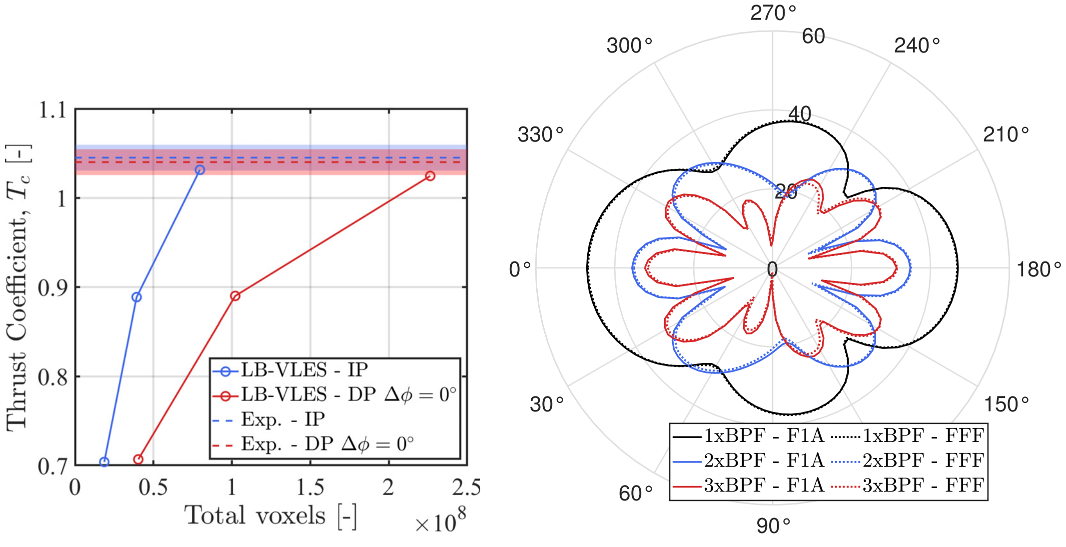

(a) (b)

FIG. 5. (a) Evolution of the thrust coefficient against the total number of voxels for the IP (blue) and the central propeller of the $\Delta\phi = 0°$ configuration (red). The experimental results for each case are shown as dashed lines, with uncertainty represented by shaded regions. (b) Comparison between LB/F1A and LB/FFF noise directivity results. L_p emitted by the central propeller of the DP configuration at $\Delta\phi = 0°$ at a distance of $100D$.

The same grid refinement strategy is applied to the DP simulations. As shown in Fig. 5(a), the case with a relative phase angle of $\Delta\phi = 0°$ (red) exhibits a deviation of 1.5% for the thrust produced by the central propeller. Moreover, torque coefficients defined as $Q_c = Q/(q_\infty \pi R^3)$, where Q is the torque given in [N m] units, are also computed for the fine grids of the IP and DP cases, reporting values of 0.683 and 0.686, respectively. When compared to the experimental values in (de Vries *et al.*, 2021), the percentage difference is 2.354% and 1.97%, respectively. The accuracy achieved in the time-averaged thrust and torque predictions is deemed sufficient to conclude that the selected grids are adequately refined to capture the aeroacoustic mechanisms under investigation. The finest grid is consequently used for all subsequent analyses.

B. Validation of far-field dipole formulation

The present section aims to validate the frequency-domain rotating-dipole far-field formulation (FFF) presented in Sec. II C against the acoustic results computed by the time-domain F1A formulation implemented in PowerACOUSTICS®. Figure 5(b) shows the directivity of the SPL calculated for the DP case with a phase angle of $\Delta\phi = 0°$ at the first, second, and third BPF harmonics. L_p is computed on the XY plane at $100D$ distance from the GRS origin: this distance will be utilized for all subsequent results presented in the following. The figure includes the noise emitted by the central propeller only. The comparison between the two methodologies shows an excellent agreement with a difference way below 1 dB in most directions. Convergence tests, not reported here, are performed to ensure that, for both formulations, the directivities do not change when considering the last three, five, or seven recorded rotations with respect to the whole recorded signal length of ten rotations. Moreover, the agreement confirms that the assumption of compactness made with FFF is respected, considering that F1A does not rely on this assumption. According to propeller noise theory (Goldstein, 1976), loading and thickness noise may be present for interacting propellers with the unsteady loading dominating at low Mach number. While the contributions of steady and unsteady loading noise are addressed in Sec. V A, only F1A also considers thickness noise in its implementation. Thanks to the obtained agreement, it is inferred that for these DEP configurations, thickness noise is negligible.

IV. AERODYNAMIC RESULTS

A. Tip-vortex evolution

Figure 6(a) illustrates the development of the slipstream for the IP case at a specific time, visualized using the λ_2 criterion, with a value of $\lambda_2 = -2 \times 10^6$ 1/s^2. The vortical structures are observed to follow a helical trajectory originating from the blade tip and continuing downstream of the rotor with minimal disturbance.

In the case of the DP configuration with $\Delta\phi = 0°$, shown in Fig. 6(b), each slipstream exhibits a similar pattern, maintaining its coherence without merging or breaking up, consistent with the experimental findings reported in de Vries *et al.* (2021). However, the proximity of the rotors causes a noticeable deformation of the vortex structures, which becomes increasingly evident further downstream of the rotor. This deformation arises following the tip-to-tip interaction and is then enhanced moving downstream by the mutual interaction of the vortical structures. The circulation around each vortex structure influences the trajectories of adjacent structures through the induced velocity field generated by their interaction. Referring to the DP case with

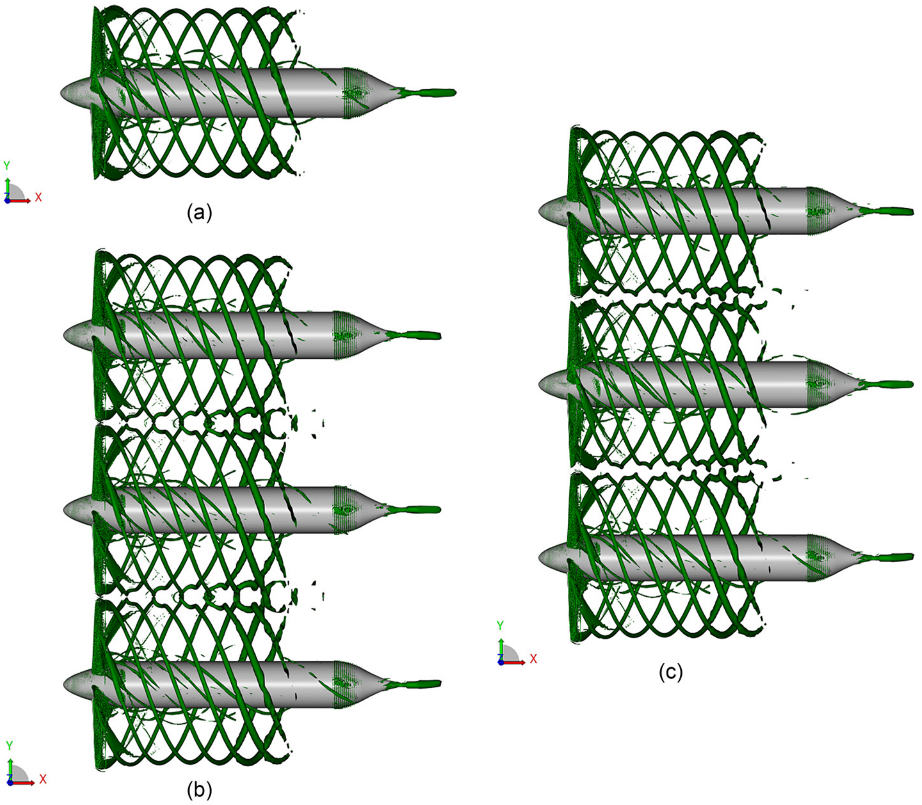

FIG. 6. Isosurface computed through the $\lambda 2$ criterion with a value of $\lambda_2 = -2 \times 10^6$ 1/s^2: isolated-propeller case (a), distributed-propeller case with $\Delta\phi = 0°$ (b), distributed-propeller case with $\Delta\phi = 30°$ (c).

$\Delta\phi = 30°$ shown in Fig. 6(c), the vortical structures maintain their helical shape similar to the previous configurations, but their relative positioning changes due to the phase shift between the rotors. This phase difference causes the wakes from adjacent rotors to be out of alignment, reducing the direct interaction between the vortices. As a result, the deformation observed in the $\Delta\phi = 30°$ case is less pronounced, and the vortices remain coherent further downstream. The evolution of the slipstreams of the other analyzed DP cases falls in between these two extremes, $\Delta\phi = 0°$ representing the case where the slipstreams are deformed the most. Conversely, $\Delta\phi = 30°$ is the case where they are deformed the least, considering that propellers with six blades are used.

B. Unsteady force distribution

This section examines the unsteady aerodynamic load per unit span generated on the central rotor due to its interaction with the adjacent ones. Figure 7(a) considers case $\Delta\phi = 0°$, showing the azimuthal distribution of the unsteady loading on the rotor disk, with the mean value subtracted. The unsteady axial load is illustrated, corresponding to the unsteady thrust produced by the propeller. The radial and

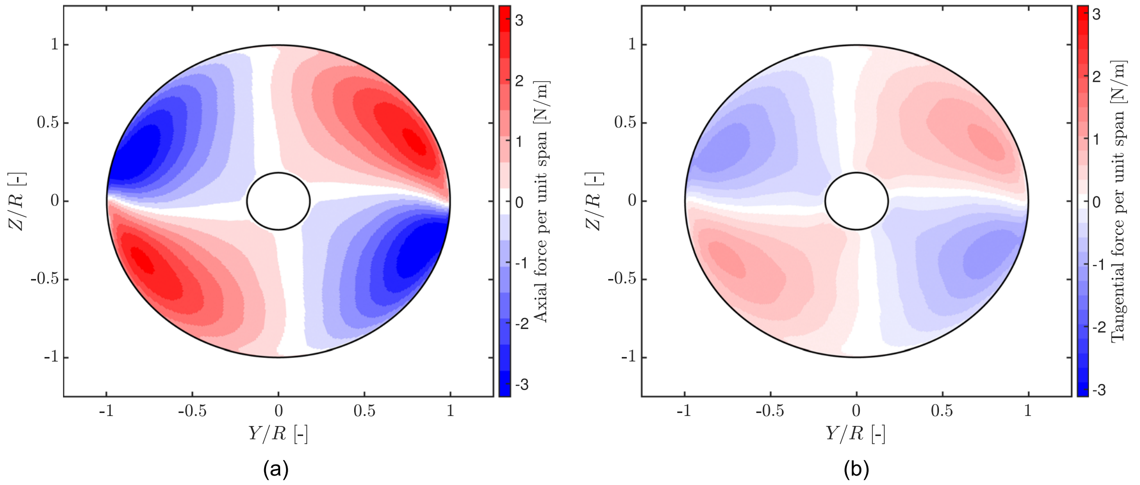

FIG. 7. Unsteady loading distribution of the central propeller for the DP case with $\Delta\phi = 0°$. Axial forces (a) and tangential forces (b).

azimuthal coordinates are divided into 180 segments, over which the local axial force is integrated to obtain this result (following Sec. II D). In the azimuthal direction, two positive thrust peaks and two negative peaks are observed, resulting from the mutual interaction with the two adjacent propellers. The points of maximum and minimum thrust are located around 85% of the radial distance from the disk center. Figure 7(b) depicts the unsteady disk loading of the tangential forces per unit span, which is obtained similarly to Fig. 7(a), and depicts a peak location around the same radial distance. Indeed, the tangential forces exhibit a qualitatively similar radial and azimuthal pattern as the axial forces, with two maximum and two minimum peaks. However, the magnitudes of the tangential forces are lower than those of the axial forces; for instance, the maximum positive peak of the axial force distribution is three times the one found on the tangential forces. Despite their lower magnitude, the tangential forces are of interest due to their significant contribution in certain directions of sound emission, as discussed in Sec. V D.

The analysis can focus on the dominant axial component to investigate the effect of the phase angle on the unsteady loading. The unsteady axial force is decomposed into a series of BLHs, following the methodology outlined in Sec. II A, as these harmonics are essential for sound generation according to Eq. (1). Due to the symmetry of the unsteady load induced by the adjacent propellers on the central rotor, the odd-order blade loading harmonics are zero. Therefore, Fig. 8(a) presents the magnitude of the second harmonic of the axial blade loading. A comparison with Fig. 7(a) shows that the second BLH exhibits a similar azimuthal modal shape and energetic values, with two positive and two negative peaks along the azimuthal direction, displaying perfect symmetry as expected from a Fourier-transform decomposition. The distribution of the sixth harmonic of the axial blade loading is plotted next in Fig. 8(b). The Bessel function assigns this harmonic the highest value via Eq. (1) for constructing the tone at the first harmonic of the BPF. As expected, six positive and six negative peaks are observed, while the absolute values are much smaller than those of the second BLH. A similar behavior is observed for all harmonics beyond the second, across different $\Delta\phi$ values. This suggests that the second BLH contains most of the energy needed to describe the unsteady axial loading presented in Fig. 7(a). Nonetheless, this harmonic does not vary with changes in the phase angle.

To demonstrate this, Fig. 9(a) integrates the value of the second harmonic along the radial direction and plots it as a function of the azimuthal coordinate. This is done for all cases with different $\Delta\phi$ analyzed in this study. It is clear that all curves perfectly overlap, their maximum difference being below 9.5×10^{-04} N. Therefore, the leading effect of $\Delta\phi$ on the unsteady loading must reside in harmonics higher than the second. This is indeed confirmed in Fig. 9(b), where the radially integrated distribution of the sixth harmonic from Fig. 8(b) is plotted for different phase angles, exhibiting significant differences among cases. This observation may explain the hypothesis put forward in de Vries *et al.* (2021), according to which two distinct sources of unsteady loading due to the interactions among adjacent rotors can exist. The first source is associated with time-averaged inflow velocities induced by the neighboring propeller. This type of loading would exist even if the adjacent propellers were modeled as idealized actuator disks with an infinite number of blades. The second source is linked to more localized, impulsive changes in loading at the blade tips. These impulsive changes occur during each blade passage through the unsteady flow field created by the finite number of blades on the adjacent propeller, particularly when the rotors are synchronized at a specific phase angle. It was noticed that this impulsive loading had no significant impact on overall propeller performance but may lead to increased noise because of the rapid changes in loading.

The analysis of the second and sixth BLHs from the present study aligns with these observations. The second harmonic, which reflects unsteady loading effects resulting from the proximity of adjacent propellers, is primarily influenced by the time-averaged interactions. As shown in Figs. 8(a) and 8(b), this harmonic shows little sensitivity to changes in the phase angle difference, $\Delta\phi$. The consistent

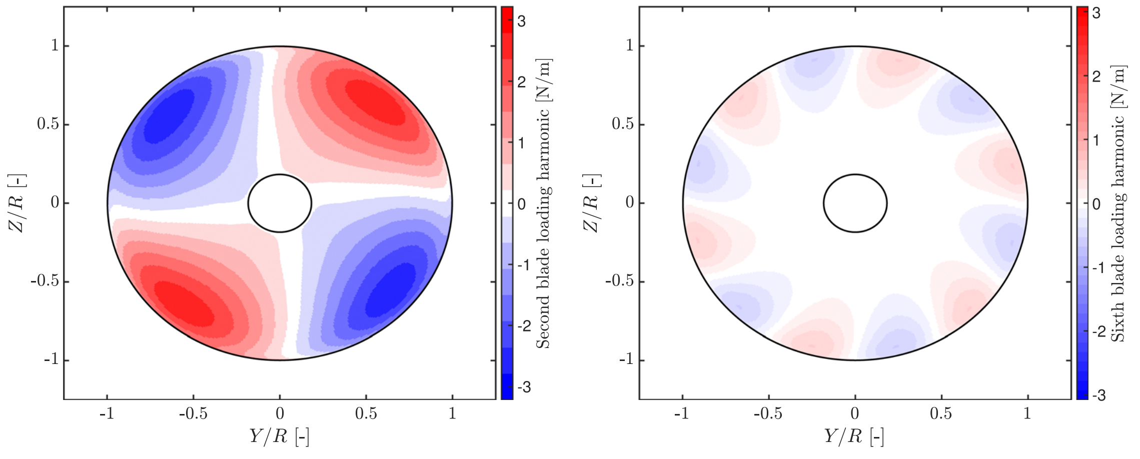

(a)

(b)

FIG. 8. Second (a) and sixth (b) blade loading harmonic magnitude of the axial force for the DP case with $\Delta\phi = 0°$. The central propeller is considered.

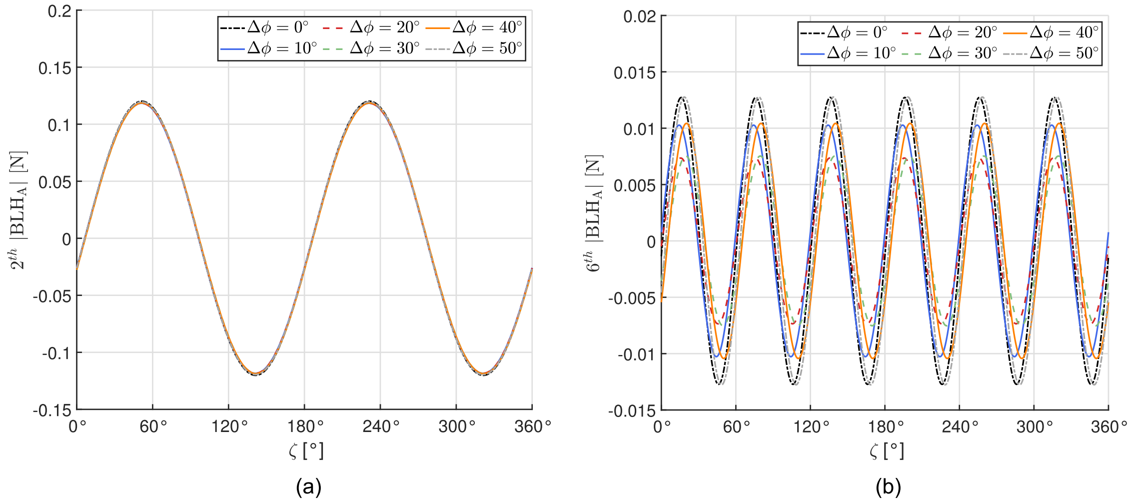

FIG. 9. Second (a) and sixth (b) blade loading harmonic magnitude of the spanwise integrated axial force for all DP cases considered. The central propeller is considered.

pattern across different phase angles suggests that the second harmonic represents a periodic loading effect due to steady inflow distortion that persists regardless of the specific angular alignment between rotors.

On the other hand, higher-order harmonics capture the more phase-dependent, impulsive loading. As illustrated in Fig. 8(b), the magnitude of the sixth harmonic varies significantly with changes in $\Delta\phi$, indicating that this harmonic is sensitive to the synchronization of the wake structures between adjacent propellers. The impulsive forces associated with this harmonic result from repeated exposures of the blades to specific parts of the unsteady flow field induced by the neighboring propellers, which vary with the relative phase angle.

V. ACOUSTIC RESULTS

A. Steady vs unsteady loading noise contributions

This section aims to determine the relative contributions of steady and unsteady loading noise in generating the tone at the BPF. The literature often assumes that the BPF tone is predominantly influenced by steady loading noise, which is closely tied to the propeller's aerodynamic performance (Sarikaya *et al.*, 2024). To address this, the focus is placed on the $\Delta\phi = 0°$ case, one of the analyzed scenarios, although similar conclusions can be extended to the other cases. For this investigation, the same spherical distribution of microphones used in Sec. II B is employed to capture the three-dimensional directivity of sound emitted by the central propeller. Acoustic interference from other propellers is excluded, allowing for a focus on the directivity caused purely by aerodynamic interactions with adjacent rotors. In Fig. 10(a), the steady loading noise contribution is isolated by considering only the terms related to the zeroth BLH in Eq. (1) (time-averaged contribution), revealing that the primary sound emission occurs in the rotor plane, with the characteristic doughnut-shaped directivity. In contrast, Fig. 10(b) presents the unsteady loading noise contribution for the $\Delta\phi = 0°$ case, showing an increase in directivity along the X axis, both upstream and downstream of the propeller,

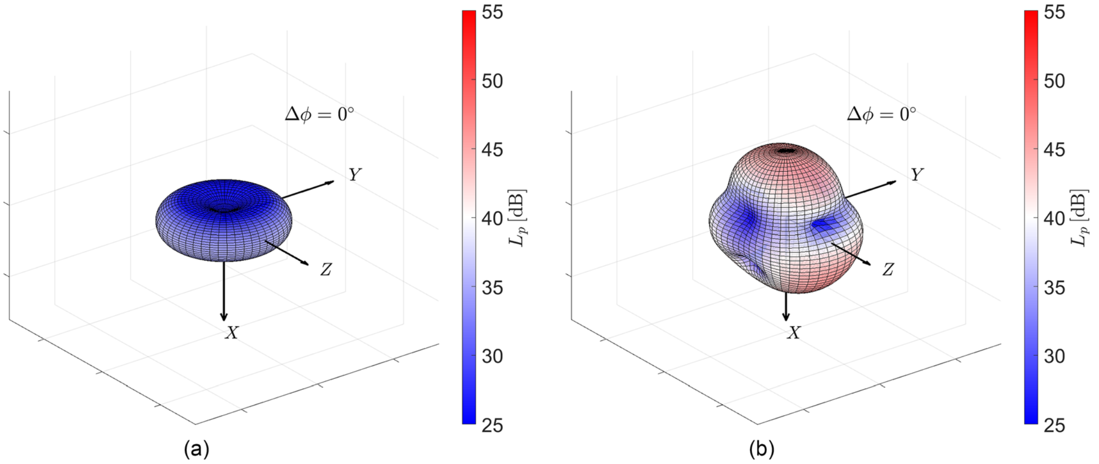

FIG. 10. Three-dimensional L_p directivity of the first BPF harmonic tone for the DP case with $\Delta\phi = 0°$. Only the contribution of the central propeller is accounted for. (a) Considering the steady loading contribution and (b) considering the unsteady loading contribution.

by up to 46.7 dB. Notably, other directions also experience increased sound levels, except along the *Y* axis. Along this axis, steady and unsteady loading noise contributions are comparable. This underscores the importance of evaluating sound emissions in a three-dimensional context instead of relying on a few strategically placed microphones, as is often the case in experimental setups constrained by space, time, or cost. It is important to note that, if considering the sound emitted by an IP, including both steady and unsteady loading noise contributions, the directivity pattern would be almost identical to that in Fig. 10(a), with differences of less than 1 dB in all directions. This confirms that steady loading noise is the dominant contributor for an IP operating in uniform flow with zero incidence angle. However, aerodynamic interaction becomes the dominant mechanism for a central propeller interacting with adjacent rotors, influencing sound generation and directivity in most directions.

Hence, the study shows that for this particular setup, the steady loading noise contribution to the BPF harmonic is marginal in most directions, although this is partly due to the use of six-blade propellers. Following Eq. (1), the Bessel function's weight for a given BLH reaches its maximum at the considered tone. For example, with six blades, the peak contribution to the BPF harmonic is assigned to the sixth BLH. As the tone's frequency increases, for instance by increasing the number of blades, the contribution from the zeroth-order BLH gradually diminishes. Therefore, for instance, two-bladed propellers working at the same advanced ratio and producing the same aerodynamic performance per blade might show a different balance between steady and unsteady noise contributions.

B. Acoustically dominant force components

The next step is to determine which force components between axial forces (related to thrust) or tangential forces (related to torque) contribute most to the directivity observed at the BPF. Radial forces are found to have a negligible impact compared to axial and tangential ones, with their contribution consistently below 1 dB in all directions. Therefore, they are excluded from the comparison. Figure 11(a) illustrates the sound generated solely by axial forces, showing that these are responsible for the increased sound levels in the upstream and downstream directions due to aerodynamic interaction, while they contribute little to emissions in the rotor plane. On the other hand, Fig. 11(b) shows that the directivity caused by tangential forces exhibits lobes in the rotor plane but does not contribute along the *X* axis.

From these observations, it is clear that despite the typically larger magnitude of axial forces (as reported in Sec. IV B), both axial and tangential forces must be considered, as they dominate sound generation in complementary spatial regions. When combining steady and unsteady force components, the overall directivity of the tone emitted at the BPF for the central propeller in the $\Delta\phi = 0^\circ$ case is observed [see Fig. 12(a)]. Again, the primary contributions remain along the *X* axis as well as along the *Z* axis.

C. Aerodynamic installation effects

The next focus is on the effect of varying the phase angle ($\Delta\phi$) on aerodynamic installation effects, without considering acoustic interference between propellers. Here, the sound contributions from the central propeller alone are considered, and the SWL is calculated as described in Sec. II. In Fig. 12(b), SWL reaches a maximum of 80.5 dB for the BPF harmonic in the $\Delta\phi = 0^\circ$ and $\Delta\phi = 50^\circ$ cases, while the minimum is observed in the $\Delta\phi = 20^\circ$ and $\Delta\phi = 30^\circ$ cases, at approximately 77.2 dB. SWL is also calculated for the second and third BPF harmonics, showing that the BPF harmonic consistently exceeds the second and third ones by at least 8.5 dB of acoustic power. Therefore, the analysis in this article focuses on the first BPF harmonic. Figure 13(a) shows the directivity obtained starting from Fig. 12(a), restricted to the distribution of microphones in the *XY* plane. It reveals that the directivity patterns across cases with varying phase angles are very similar to that of $\Delta\phi = 0^\circ$. Specifically, within the angular ranges from 60° to 120° and from 240° to 300°, all cases exhibit similar values, with differences of less than 1.5 dB. This is the region where steady

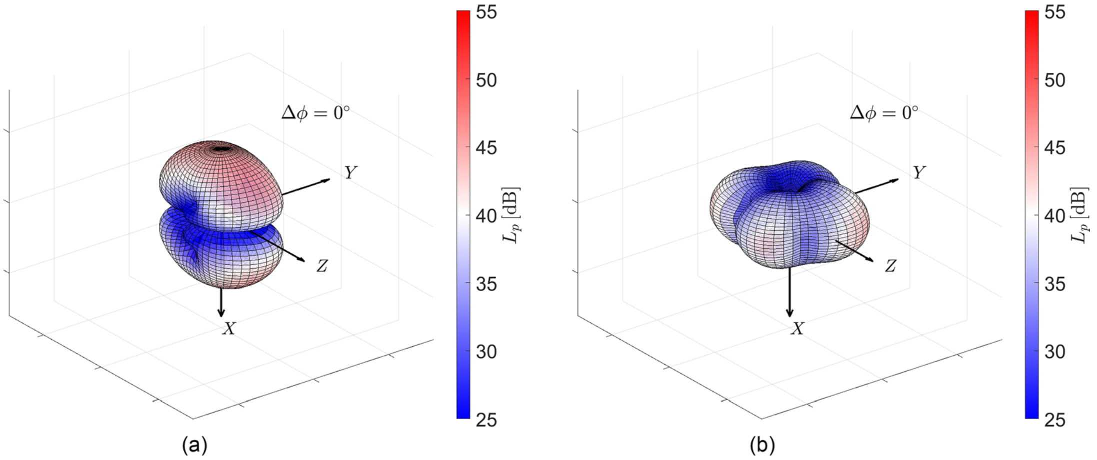

FIG. 11. Three-dimensional L_p directivity of the first BPF harmonic tone for the DP case with $\Delta\phi = 0^\circ$. Only the contribution of the central propeller is accounted for. (a) Considering the axial loading contribution and (b) considering the tangential loading contribution.

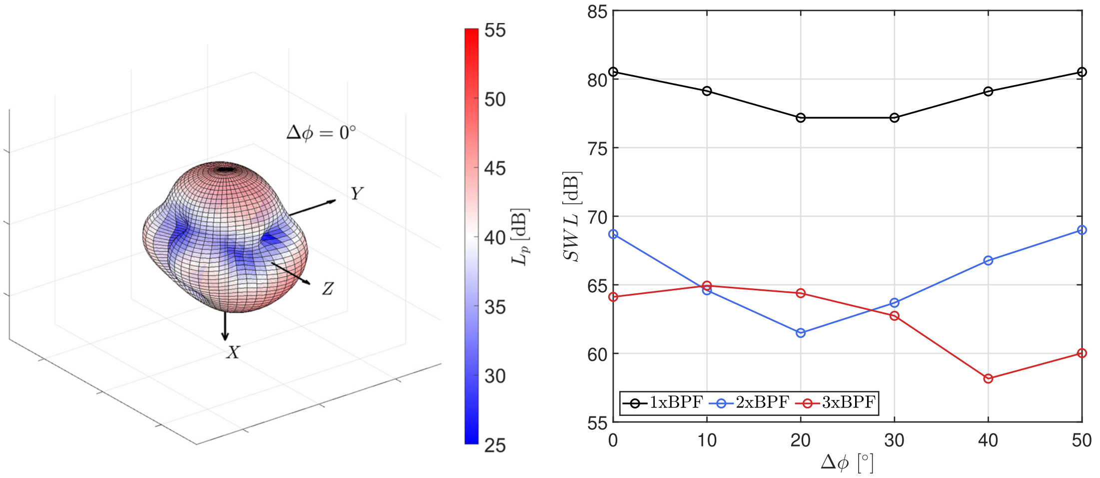

(a)

(b)

FIG. 12. Noise directivity of the DP central propeller contribution. (a) Three-dimensional L_p directivity of the first BPF harmonic tone for the DP case with $\Delta\phi = 0°$. (b) SWL trends for the tones at the first, second, and third BPF harmonics for different phase angles.

loading noise contributes significantly, as indicated in Fig. 10(a), and where the aerodynamic performance of the rotors remains largely unaffected by changes in phase angle.

However, differences emerge along the X axis (0° to 180°), where the unsteady axial force component dominates. Interestingly, in the regions upstream and downstream of the propellers, the SPL in the $\Delta\phi = 0°$ and $\Delta\phi = 50°$ cases are nearly identical, with differences of less than 1 dB. At the same time, the $\Delta\phi = 20°$ and $\Delta\phi = 30°$ cases, as well as the $\Delta\phi = 10°$ and $\Delta\phi = 40°$ cases, behave similarly. The exact cause of this phenomenon is unclear, but a potential explanation can be found in the harmonic content of the axial force. Figure 9(b) shows that the sixth BLH for the paired cases (varied by $\Delta\phi$) exhibits similar peak-to-peak values, leading to the nearly overlapping results reported in Fig. 13(a). This suggests that the observed effect is not due to acoustic interference between the central rotor's blades but rather to the harmonics of the axial force. A more thorough analysis, involving flow velocity components and the local blade angle of attack, would be necessary to provide more physical insight into this interesting behavior. However, this investigation lies beyond the scope of the current study and will be addressed in future research.

Figure 13(b) is analogous to the previous figure but shows the microphone distribution in the XZ plane. Again, the pairing behavior discussed earlier is evident in the regions along the X axis (0° to 180°), where the unsteady axial force component dominates BPF harmonic emissions. Although the SPLs vary with $\Delta\phi$, the overall three-dimensional directivity remains consistent, indicating that the underlying sound generation mechanisms are similar, and only the intensity is modulated by the phase angle.

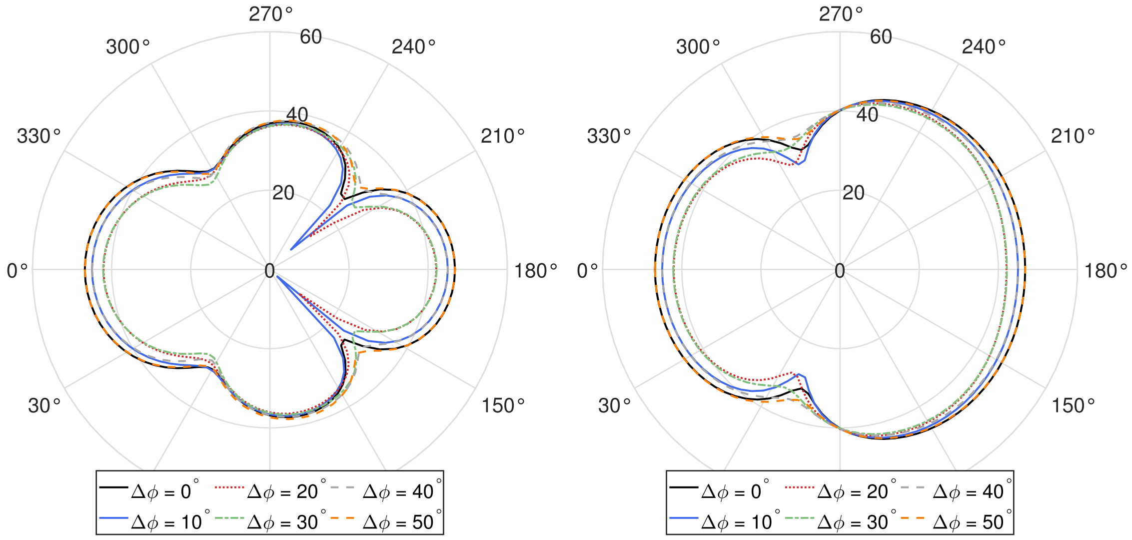

(a)

(b)

FIG. 13. Far-field sound L_p directivity comparing the distributed central propeller cases for different phase angles. The first BPF harmonic tone is depicted. Microphones distributed in the XY (a) and XZ (b) planes, respectively.

D. Acoustic installation effects

The spatial directivity of sound is analyzed while accounting for acoustic interference between adjacent rotors. Figure 14(a) presents the directivity for the BPF tone, accounting for the contributions from all three rotors for the $\Delta\phi = 0^\circ$ case. The directivity is altered compared to the central propeller-only case [Fig. 12(a)], with the X and Z axes still exhibiting the highest emissions, while the Y axis shows a lobed pattern with significantly lower SPL peaks.

Figure 14(b) shows the SWL variation with phase angle when all three rotors' contributions are included. The $\Delta\phi = 0^\circ$ case shows a maximum SWL of 85.7 dB at the BPF harmonic, while the $\Delta\phi = 30^\circ$ case reaches a minimum of 78.2 dB. For the $\Delta\phi = 30^\circ$ case, the BPF harmonic exceeds the second and third harmonics by 9.3 dB and 17.2 dB, respectively, and even larger differences are observed in other cases. Thus, the focus remains on the first BPF harmonic when analyzing acoustic interference between rotors. The phase angle also significantly impacts the spatial directivity's level and shape due to acoustic interference, as shown in Fig. 15(a), where microphones are distributed 100 diameters from the GRS origin in the XY plane.

The $\Delta\phi = 0^\circ$ and $\Delta\phi = 30^\circ$ cases demonstrate opposite directivity patterns. In the $\Delta\phi = 0^\circ$ case, the maximum SPL occurs along the X axis (0° to 180°), with values of about 52.7 dB, while emissions along the Y axis (90° to 270°) are much lower than 19 dB. Conversely, in the $\Delta\phi = 30^\circ$ case, the highest SPL occurs along the Y axis, with values reaching 41.9 dB, while the X axis emissions are below 10 dB. These results confirm that acoustic interference between rotors plays a significant role in shaping the spatial directivity of sound, even when a strong aerodynamic interaction is present among propellers. This conclusion is further supported by Fig. 15(b), which shows the directivity in the XZ plane. Here, while all cases depict similar SPL directivity shapes with varying $\Delta\phi$, the most remarkable result is obtained for the $\Delta\phi = 30^\circ$ case. The effect of the acoustic interference is to drastically reduce the acoustic emissions in every direction, yielding a dipolar directivity pattern that peaks along the Z axis (90° to 270°) around 36 dB. This means that the significant contribution generated by the aerodynamic installation in front and behind the propellers (0° to 180°), previously discussed and illustrated in Fig. 13(b), is here nullified by the acoustic interference among propellers.

VI. CONCLUSIONS

Insights into the acoustic and aerodynamic characteristics of co-rotating distributed electric propellers have been provided through this study. By employing high-fidelity LB simulations, the aerodynamic and noise generation mechanisms of multiple configurations were investigated. Several findings were revealed.

(1) The unsteady loading noise could be decoupled into an effect due to the time-averaged inflow distortion caused by the presence of the adjacent propellers, and one due to the impulsive local effects of the blade tip, confirming the observations made in the literature (de Vries *et al.*, 2021). The relative phase angle affects only the impulsive component of the unsteady noise, which explains why aerodynamic performance remains unchanged, as observed in previous literature work (Turhan *et al.*, 2024; Visingardi *et al.*, 2024).
(2) The aerodynamic interaction between the propellers generates the unsteady loading noise, which dominates the sound emission of DEP systems at the BPF tone. However, the steady loading noise remains important in certain spatial directions, particularly along the Y axis.
(3) Despite the tangential forces having much lower absolute values than the axial forces, both need to be considered in calculating the tonal noise at the BPF harmonic.

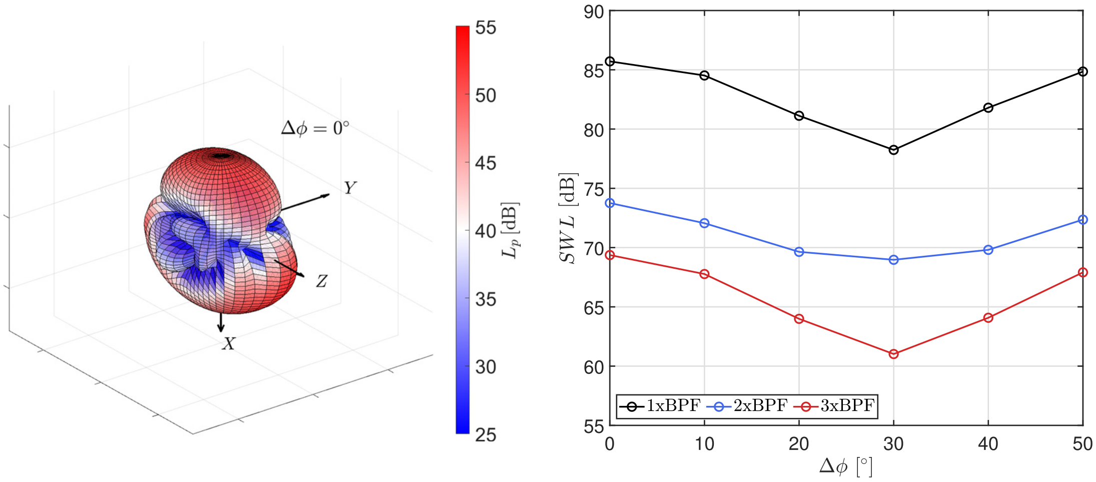

(a)

(b)

FIG. 14. (a) Three-dimensional L_p directivity of the first BPF harmonic tone for the DP case with $\Delta\phi = 0^\circ$. (b) SWL trends for the tones at the first, second, and third BPF harmonics for different phase angles. For both images, the acoustic interference effects are accounted for by including the contributions of the three propellers.

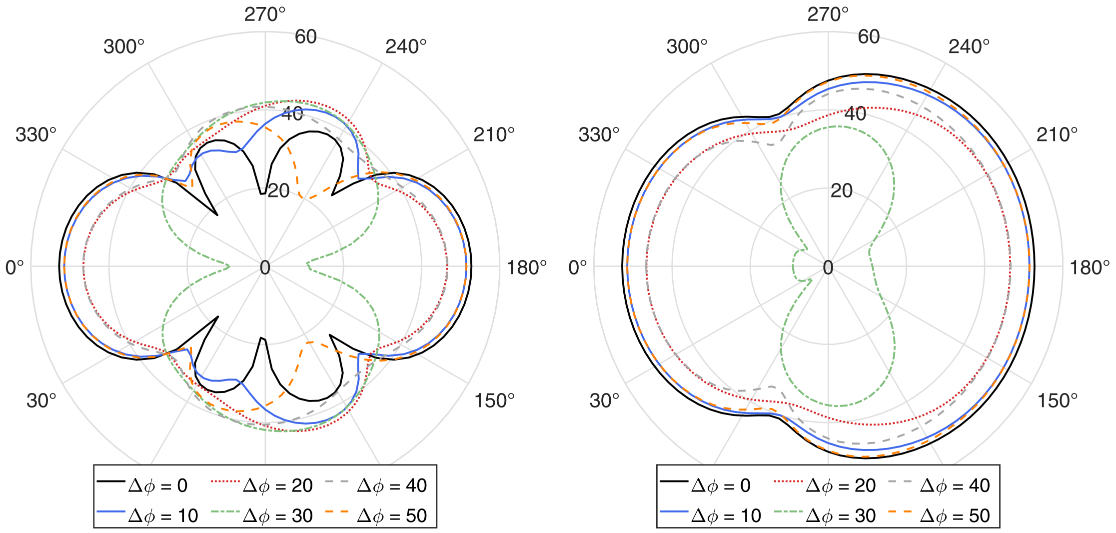

(a)

(b)

FIG. 15. Far-field sound L_p directivity comparing the DP cases varying $\Delta\phi$. The first BPF harmonic tone is depicted. The acoustic interference effects are accounted for by including the contributions of the three propellers. Microphones distributed in the *XY* (a) and *XZ* (b) planes, respectively.

These two force components contribute complementarily to sound directivity.

(4) When the effects of aerodynamic installation on the tone at the BPF harmonic are isolated, the spatial directivity pattern remains similar as $\Delta\phi$ varies. However, SPL can differ by up to 4.5 dB along the X axis, where unsteady aerodynamic interactions drive the sound.

(5) The acoustic interference between the propellers plays a crucial role in mitigating the BPF harmonic tone. The most promising result was the case with $\Delta\phi = 30°$, where destructive interference between the blades almost completely cancels the sound generation along the X axis, which is otherwise dominated by aerodynamic interactions.

Considering these findings, it is evident that destructive acoustic interference between propellers should be explored further as a potential mitigation strategy for noise reduction in realistic DEP systems. The important alterations in directivity patterns highlighted in this work likely explain the noise reductions observed in the experimental studies reported in the introduction. In fact, assessing the mitigation potential of a specific propeller array's phase angle requires more than a limited number of microphone measurements; it necessitates a comprehensive evaluation of both the SWL and the global directivity pattern. However, it must be emphasized that the primary source of tonal noise generation remains the unsteady loads caused by aerodynamic interactions. Therefore, future research should prioritize the development of low-order models that accurately capture the aerodynamic interactions between propeller slipstreams. Such models would enable the rapid assessment of various clocking angles, facilitating the identification of configurations that minimize noise emissions while maintaining aerodynamic performance. This approach would provide an efficient means of optimizing DEP systems for quieter operation in urban environments.

ACKNOWLEDGMENTS

This research was conducted as part of the H2020 Research and Innovation Actions ENODISE (ENabling Optimized DISruptivE airframe-propulsion integration concepts) and eVTOLUTION (eVTOL Multi-fidelity Hybrid Design and Optimization for Low Noise and High Aerodynamic Performance), funded by the European Commission under Grant Agreement Nos. 860103 and 101138209, respectively. The computations in this work used the Dutch national e-infrastructure with the support of the SURF Cooperative using Grant No. EINF-6653. Finally, the authors thank Mr. Jatinder Goyal (Ph.D. Candidate at TU Delft) for the inspiring technical discussions on high-fidelity computations.

AUTHOR DECLARATIONS

Conflict of Interest

The authors report no conflict of interest.

DATA AVAILABILITY

The data that support the findings of this study are available from the corresponding author upon reasonable request.

Avallone, F., Casalino, D., and Ragni, D. (**2018a**). "Impingement a propeller-slipstream a leading edge with a flow-permeable insert: A computational aeroacoustic study," Int. J. Aeroacoustics **17**(6–8), 687–711.

Avallone, F., van der Velden, W. C. P., Ragni, D., and Casalino, D. (**2018b**). "Noise reduction mechanisms of sawtooth and combed-sawtooth trailing-edge serrations," J. Fluid Mech. **848**, 560–591.

Barker, J. E., Zarri, A., Christophe, J., and Schram, C. F. (**2023**). "Numerical investigation of tonal noise emissions from propeller-wing aerodynamic and acoustic interactions," in *Proceedings of the AVIATION 2023 Forum*, June 12–16, San Diego, CA.

Bernardini, G., Centracchio, F., Gennaretti, M., Iemma, U., Pasquali, C., Poggi, C., Rossetti, M., and Serafini, J. (**2020**). "Numerical characterisation of the aeroacoustic signature of propeller arrays for distributed electric propulsion," Appl. Sci. **10**(8), 2643.

Bhatnagar, P. L., Gross, E. P., and Krook, M. (**1954**). "A model for collision processes in gases. I. Small amplitude processes in charged and neutral one-component systems," Phys. Rev. **94**, 511–525.

Casalino, D. (**2003**). "An advanced time approach for acoustic analogy predictions," J. Sound Vib. **261**, 583–612.

Casalino, D., Avallone, F., Gonzalez-Martino, I., and Ragni, D. (**2019a**). "Aeroacoustic study of a wavy stator leading edge in a realistic fan/OGV stage," J. Sound Vib. **442**, 138–154.

Casalino, D., Grande, E., Romani, G., Ragni, D., and Avallone, F. (**2021**). "Definition of a benchmark for low Reynolds number propeller aeroacoustics," Aerosp. Sci. Technol. **113**, 106707.

Casalino, D., Romani, G., Pii, L. M., and Colombo, R. (**2023**). "Flow confinement effects on sUAS rotor noise," Aerosp. Sci. Technol. **143**, 108756.

Casalino, D., Romani, G., Zhang, R., and Chen, H. (**2022**). "Lattice-Boltzmann calculations of rotor aeroacoustics in transitional boundary layer regime," Aerosp. Sci. Technol. **130**, 107953.

Casalino, D., Van der Velden, W., Romani, G., and Gonzalez-Martino, I. (**2019b**). "Aeroacoustic analysis of urban air operations using the LB/VLES method," in *Proceedings of the 25th AIAA/CEAS Aeroacoustics Conference*, May 20–23, Delft, The Netherlands.

Chen, H., Teixeira, C., and Molvig, K. (**1998**). "Realization of fluid boundary conditions via discrete boltzmann dynamics," Int. J. Mod. Phys. C **09**, 1281–1292.

De Paola, E., Camussi, R., Stoica, G., Di Marco, A., and Capobianchi, G. (**2024**). "Aerodynamic and aeroacoustic experimental investigation of a three propellers DEP configuration," Aerosp. Sci. Technol. **154**, 109508.

de Vries, R., van Arnhem, N., Sinnige, T., Vos, R., and Veldhuis, L. L. (**2021**). "Aerodynamic interaction between propellers of a distributed-propulsion system in forward flight," Aerosp. Sci. Technol. **118**, 107009.

Farassat, F. (**2007**). Derivation of Formulations 1 and 1A of Farassat, Technical Memorandum No. 2007-214853 (NASA, Hampton, Virginia).

Glegg, S., and Devenport, W. (**2017**). *Aeroacoustics of Low Mach Number Flows: Fundamentals, Analysis, and Measurement* (Elsevier, Amsterdam).

Goldstein, M. E. (**1976**). *Aeroacoustics* (McGraw-Hill, New York).

Goyal, J., Sinnige, T., Avallone, F., and Ferreira, C. (**2024**). "Benchmarking of aerodynamic models for isolated propellers operating at positive and negative thrust," AIAA J. **62**, 3758–3775.

Guan, S., Lu, Y., Su, T., and Xu, X. (**2021**). "Noise attenuation of quadrotor using phase synchronization method," Aerosp. Sci. Technol. **118**, 107018.

Hanson, D. (**1976**). "Near field noise of high tip speed propellers in forward flight," in *Proceedings of the 3rd Aeroacoustics Conference*, July 20–23, Palo Alto, CA.

Intaratep, N., Alexander, W. N., Devenport, W. J., Grace, S. M., and Dropkin, A. (**2016**). "Experimental study of quadcopter acoustics and performance at static thrust conditions," in *Proceedings 22nd AIAA/CEAS Aeroacoustics Conference, American Institute of Aeronautics and Astronautics*, May 30–June 1, Lyon, France.

Kim, H. D., Perry, A. T., and Ansell, P. J. (**2018**). "A review of distributed electric propulsion concepts for air vehicle technology," in *Proceedings of the 2018 AIAA/IEEE Electric Aircraft Technologies Symposium (EATS)*, July 12–14, Cincinnati, OH.

Kummer, J., and Dang, T. (**2006**). "High-lift propulsive airfoil with integrated crossflow fan," J. Aircraft **43**, 1059–1068.

Lee, H., and Lee, D.-J. (**2020**). "Rotor interactional effects on aerodynamic and noise characteristics of a small multirotor unmanned aerial vehicle," Phys. Fluids **32**(4), 047107.

NASA (**2017**). Strategic Implementation Plan: 2017 Update (NASA, Washington, DC). https://www.nasa.gov/sites/default/files/atoms/files/sip-2017-03-23-17-high.pdf (Last viewed April 20, 2025).

Nie, X., Shan, X., and Chen, H. (**2009**). "A lattice-Boltzmann / finite-difference hybrid simulation of transonic flow," in *Proceedings of 47th AIAA Aerospace Sciences Meeting including The New Horizons Forum and Aerospace Exposition*, January 5–8, Orlando, FL.

Pascioni, K., and Rizzi, S. A. (**2018**). "Tonal noise prediction of a distributed propulsion unmanned aerial vehicle," in *Proceedings of the 2018 AIAA/CEAS Aeroacoustics Conference*, June 25–29, Atlanta, GA.

Pascioni, K. A., Rizzi, S. A., and Schiller, N. (**2019**). "Noise reduction potential of phase control for distributed propulsion vehicles," in *Proceedings of the AIAA Scitech 2019 Forum*, January 7–11, San Diego, CA.

Patterson, A., Schiller, N. H., Ackerman, K. A., Gahlawat, A., Gregory, I. M., and Hovakimyan, N. (**2020**). "Controller design for propeller phase synchronization with aeroacoustic performance metrics," in *Proceedings of the AIAA Scitech 2020 Forum*, January 6–10, Orlando, FL.

Roger, M., Acevedo-Giraldo, D., and Jacob, M. C. (**2022**). "Acoustic versus aerodynamic installation effects on a generic propeller-driven flying architecture," Int. J. Aeroacoustics **21**(5–7), 585–609.

Roger, M., and Moreau, S. (**2020**). "Tonal-noise assessment of quadrotor-type UAV using source-mode expansions," Acoustics **2**(3), 674–690.

Romani, G., and Casalino, D. (**2019**). "Rotorcraft blade-vortex interaction noise prediction using the lattice-Boltzmann method," Aerosp. Sci. Technol. **88**, 147–157.

Romani, G., Grande, E., Avallone, F., Ragni, D., and Casalino, D. (**2022a**). "Computational study of flow incidence effects on the aeroacoustics of low blade-tip Mach number propellers," Aerosp. Sci. Technol. **120**, 107275.

Romani, G., Grande, E., Avallone, F., Ragni, D., and Casalino, D. (**2022b**). "Performance and noise prediction of low-Reynolds number propellers using the lattice-Boltzmann method," Aerosp. Sci. Technol. **125**, 107086.

Sarikaya, B., Zarri, A., Christophe, J., Aissa, M. H., Verstraete, T., and Schram, C. (**2024**). "Aerodynamic and aeroacoustic design optimization of UAVs using a surrogate model," J. Sound Vib. **589**, 118539.

Schram, C. (**2011**). "Ffowcs Williams & Hawkings analogy" Lecture Notes, von Karman Institute for Fluid Dynamics, Sint-Genesius-Rode, Belgium.

Shan, X., and Chen, H. (**2006**). "Kinetic theory representation of hydrodynamics: A way beyond the navier-stokes equation," J. Fluid Mech. **550**, 413–441.

Shao, M., Lu, Y., Xu, X., Guan, S., and Lu, J. (**2022**). "Experimental study on noise reduction of multi-rotor by phase synchronization," J. Sound Vib. **539**, 117199.

Teets, E. H., Jr., Donohue, C. J., Wright, P. T., and DelFrate, J. (**2002**). Meteorological support of the Helios world record high altitude flight to 96,863 feet, Technical Memorandum No. 2002-210727 (NASA, Washington, DC).

Torija, A. J., Chaitanya, P., and Li, Z. (**2021**). "Psychoacoustic analysis of contra-rotating propeller noise for unmanned aerial vehicles," J. Acoust. Soc. Am. **149**(2), 835–846.

Turhan, B., Jawahar, H. K., Gautam, A., Syed, S., Vakil, G., Rezgui, D., and Azarpeyvand, M. (**2024**). "Acoustic characteristics of phase-synchronized adjacent propellers," J. Acoust. Soc. Am. **155**(5), 3242–3253.

Visingardi, A., Barbarino, M., De Gregorio, F., Testa, C., Zaghi, S., Yin, J., Reboul, G., Cavalli, A., Granata, D., Abergo, L., Guardone, A., Zanotti, A., Bernardini, G., Poggi, C., Candeloro, P., Pagliaroli, T., Barakos, G., Qiao, G., and Muth, M. (**2024**). "Analysis of the aeroacoustic performance of twin propellers in hover by using the CIRA-Cusano test rig," in *Proceedings of the 50th European Rotorcraft Forum*, September 10–12, Marseille, France.

Yakhot, V., and Orszag, S. A. (**1986**). "Renormalization-group analysis of turbulence," Phys. Rev. Lett. **57**, 1722–1724.

Zang, B., Turhan, B., Torija, A. J., Ramos-Romero, C., and Azarpeyvand, M. (**2024**). "An acoustic and psychoacoustic assessment on the noise control of propellers in distributed propulsion configuration using phase-synchronisation," in *Proceedings of EventQuiet Drones 2024*, September 8–11, Manchester, UK.

Zarri, A., Dell'Erba, E., Munters, W., and Schram, C. (**2022a**). "Aeroacoustic installation effects in multi-rotorcraft: Numerical investigations of a small-size drone model," Aerosp. Sci. Technol. **128**, 107762.

Zarri, A., Dell'Erba, E., Munters, W., and Schram, C. (**2022b**). "Fuselage scattering effects in a hovering quadcopter drone," in *Proceedings of the 28th AIAA/CEAS Aeroacoustics 2022 Conference*, June 14–17, Southampton, UK.

Zhou, W., Ning, Z., Li, H., and Hu, H. (**2017**). "An experimental investigation on rotor-to-rotor interactions of small UAV propellers," in *Proceedings of the 35th AIAA Applied Aerodynamics Conference*, June 5–9, Denver, CO.